Plasma Chem Plasma Process (2017) 37:783–804
DOI 10.1007/s11090-017-9788-8

REVIEW ARTICLE

# Synthesis of Functional Oxide Nanoparticles Through RF Thermal Plasma Processing

**Takamasa Ishigaki**[1]

Received: 14 December 2016 / Accepted: 22 January 2017 / Published online: 30 January 2017


**Abstract** A method of synthesizing functional nanostructured powders through reactive thermal plasma processing has been developed. Nano-sized oxide powders, including titanium dioxide and some functional oxides, were synthesized by the oxidation of liquid precursors. Oxides with the prescribed cation ratio of the liquid precursor can be synthesized with this technique, and it is possible to precisely adjust the chemical composition, which is linked to the appropriate functions of ceramic materials. Quench gases, either injected from the shoulder of the reactor or injected counter to the plasma plume from the bottom of the reactor, were used to vary the quench rate; therefore, the particle size of the resultant powders. The experimental results are well supported by numerical analysis on the effects of quench gases on the flow pattern and temperature field of thermal plasma as well as on the trajectory and temperature history of particles. Plasma-synthesized $TiO_2$ nanoparticles showed phase preferences different from those synthesized by conventional wet-chemical processes. Nano-sized particles of high crystallinity and nonequilibrium chemical composition were formed in one step via reactive thermal plasma processing. The plasma-synthesized nanoparticles were spherical and hardly agglomerated, and high dispersion properties were observed, i.e., the plasma-synthesized $TiO_2$ nanoparticles were individually dispersed in water.

**Keywords** Nano-sized particle · Thermal plasma processing · Non-equilibrium chemical composition · Metastable phase · Phase formation · Optical and photocatalytic properties · Dispersibility

In honor of Emeritus Professor Emil Pfender.

✉ Takamasa Ishigaki
ishigaki@hosei.ac.jp

[1] Department of Chemical Science and Technology, Hosei University, 3-7-2 Kajino-cho, Koganei-shi, Tokyo 184-8584, Japan

## Introduction

Nanoparticles offer one possibility for the breakthrough needed to advance the conversion of substances to materials [1]. Toward the materialization of nanoparticles, the advantages of nanoparticles may be described from two points of view. One is the so-called "nanosize effect" expected in physical properties, such as luminescence, or chemical properties such as catalytic activity. The other is the resource effect, which reduces the volume of materials required for functionalization. In both cases, the primary requirement is to homogeneously produce highly functional substances in large volumes. If this is achieved, the materialization of nanoparticles is possible.

The current situation, however, is that the properties of nanoparticles have not yet attained to their best. To effectively utilize the properties of nanoparticles, it will be important to control crystallinity and surface properties as well as the homogeneity of crystallite size and chemical composition.

Powder synthesis should be carried out to precisely control particle size, morphology, chemical composition, etc.… A monodispersed powder is defined to have a standard deviation of below 10%. Conventionally synthesized nanopowders, however, hardly satisfy this requirement. The morphology and chemical composition of particles are closely related to particle assembly and functionalization. Control of surface properties is essential to the application of nanoparticles in functional ordered-arrays. Dispersed structures also require controlled surface properties.

Nanoparticle synthesis of ceramic materials has conventionally been achieved by solution processes. Taking the example of luminescence properties, major factors that have hindered the functionalization of solution-synthesized oxide nanoparticles include low crystallinity, quenching by surface hydroxyl groups, incomplete composition control (doping concentration, surface segregation), etc.. Moreover, the existence of surface hydroxyls is known to have a large impact on the dispersion of nanoparticles in a solvent.

Thermal plasma of high temperatures exceeding 10,000 K has been effectively used to synthesize nanocrystalline powders. The synthesis began through an important contribution by Emeritus Professor Pfender, University of Minnesota.

In this review paper, thermal plasma materials processing and its characteristic, and then its advantages in nanoparticle synthesis are first described. Next, research achievements thorough the liquid precursor injection into radio frequency (RF) induction plasma are discussed, with the aim of materializing highly functional nanoparticles synthesized with plasma.

## Synthesis of Ceramic Nanoparticles in Reactive Thermal Plasmas

Thermal plasmas possess many advantages and provide unique reaction fields for materials processing. The improved controllability of the reaction fields, in which chemical reactions proceed to yield materials, should lead to the synthesis of unique materials with respect to morphology, crystal structure, and chemical composition [2, 3]. Arc discharge, which is a thermal plasma, proves to be a useful tool in the synthesis and surface modification of a wide range of metals and inorganic materials. Its advantages as a reaction field are as follows. (1) Thermal plasmas have quite high temperatures (up to <15,000 K). As the plasmas are generated at relatively high pressures (close to atmospheric pressure), they have large densities and considered to be at equilibrium (local thermal equilibrium). That

is, the temperatures of heavy particles (such as atoms, molecules, and ions) are almost equal to that of light species (i.e., electrons). (2) High concentrations of chemically reactive radicals enhance the reactivity of thermal plasmas. (3) Superfast quenching ($<10^5$ to $<10^6$ K/s) takes place in the plasma tail flame region.

A representative industrial use of thermal plasma processing is the spheroidization of materials with high melting temperatures and large particle sizes (e.g., 50–100 μm). Figure 1 shows the spheroidized micron-size particles of titanium carbide, which has a melting temperature higher than 3500 K [4]. In fact, 30 kg of refractory tungsten metal particles can be treated per hour, which corresponds to 1 ton per week [5]. As thermal plasma processing has inherent characteristics, i.e., processing at an industrially acceptable production rate, ongoing studies on nano-structure control of materials using thermal plasma technology would also make it possible for extended practical applications of nano-sized functional particles in a short time.

Nano-sized particles are formed by a process of rapid quenching and condensation after precursors are supplied to thermal plasma and instantaneously evaporated. The rapid temperature decrease in the tail flame gives rise to supersaturation in a vapor phase, after which the nucleation process takes place. In the same way, the rapid cooling suppresses grain growth; therefore, nanoparticles below 100 nm in size are produced without difficulty. Advanced technologies should be pursued to control the plasma reaction fields to yield (a) high production rates, (b) reduction of particle size and narrowing of size distribution, and (c) high crystallinity and phase control. Practical applications of nano-sized particles would be possible as long as such technologies exist.

Synthesis of ceramic nano-sized powders, called ultra-fine powders in the 1980–1990s, using thermal plasmas gained much attention in the fabrication of more easily sinterable non-oxide powders, such as SiC and $Si_3N_4$. High-density sintered bodies of these materials were expected for engineering ceramic materials, which could be used at higher temperatures than metals. Pioneering studies headed by Professor Pfender demonstrated the synthesis of SiC and $Si_3N_4$ in direct current (DC) arc plasmas [6–9]. Studies on ultra-fine-powder synthesis of Si-based materials followed using RF-DC hybrid [10, 11] and RF [12–15] thermal plasmas. Also, hypersonic plasma particle deposition system, in which modified DC plasma torch was employed, showed in situ fabrication of free-standing bodies composed of nano-size grains [16].

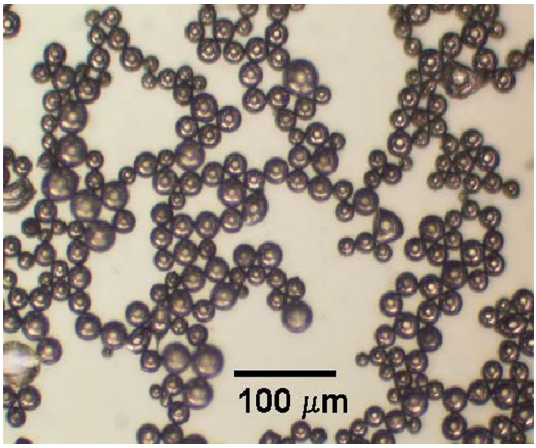


**Fig. 1** Spherical TiC particles prepared by in-flight melting and spheroidization in RF thermal plasma [4]

## Synthesis of Nano-structured Ceramic Materials Thorough Liquid Precursor Injection Into RF Induction Plasma

Thermal plasmas are mainly generated in DC arc torches and RF induction torches. Direct current arc discharges with high energy density has been widely used for various industrial applications, such as plasma spraying, plasma metallurgy, as well as the powder synthesis process [2, 3]. Compared with DC arc discharge, the RF induction plasma has more advantages. The plasma is inductively heated by an RF electrical power of tens of kW and a frequency in MHz. The diameter is 30–40 mm; therefore, the plasma volume is relatively large. The axial plasma velocity is as low as 10 m/s, and the residence time in the high-temperature plasma flame is as long as tens of ms, which is long enough for chemical reactions to proceed. The most important characteristic comes from the fact that the generation of RF induction plasma does not involve electrodes, and any gas can be used to generate the plasma, regardless of its oxidative, reductive, or reactive property. The above-mentioned characteristics of thermal plasma provide unique reaction fields for materials processing.

Flame pyrolysis [17–21] is a straightforward way to generate well-dispersed crystalline nanoparticles at an acceptable scale. It is believed that P25 powder is produced via flame oxidation of $TiCl_4$ vapor. Radio frequency thermal plasma processing has similarities to flame pyrolysis but is characterized by its much higher temperature ($\sim 10^4$ K) and fast quenching ($10^{5–6}$ K/s) at the tail part of the plasma. Nanoparticle production by using the advantages of thermal plasmas, i.e., high-temperature heat source with tremendously large enthalpy, began with the use of solid-sate precursors. Relatively coarse particles were introduced into thermal plasmas to synthesize nano-sized particles through evaporation and the subsequent coagulation processes. With this production method, problems arise from the residual coarse particles. When precursor powders are injected into a thermal plasma, in which the temperature and flow distributions exist both radially and axially, some of the precursor particles are not evaporated completely. The non-evaporated particles, though a small number, necessitate an additional post-separation process [22–24].

Injection of liquid precursors into RF induction plasma has advantages in synthesizing nano-sized functional ceramic powders. When a precursor mist with a droplet size of tens of μm is fed into a plasma having a high temperature exceeding 10,000 °C, the mist vaporizes instantaneously, enabling nanoparticle formation. Oxides with the prescribed cation ratio of the liquid precursor can be synthesized with this technique, and it is possible to adjust the chemical composition, which is linked to the appropriate functions of ceramic materials. Compositional control, such as doping content into host materials and the variable chemical composition in complex oxides, is essential to enable these functions.

The use of liquid precursor is also relatively easy compared to the mixing of gas precursors. Gas-phase synthesis of Al-doped $TiO_2$ was reported using gas-phase precursors, $TiCl_4$ and $Al_2Cl_6$ gases [25]. Mixed Ar–$TiCl_4$ gas was generated by bubbling of Ar gas in liquid $TiCl_4$ maintained at room temperature, while mixed Ar–$Al_2Cl_6$ was generated by Ar gas flowing over solid $AlCl_3$ heated at 378 K. A simplified process was conducted for the thermal plasma synthesis of Al-doped $TiO_2$ nano-sized powders by injecting an $AlCl_3$-dissolved methanol solution into Ar-$O_2$ plasma together with Ar–$TiCl_4$ gas [26].

Precise synthesis of functional oxide was reported with the injection of aqueous solution precursors into Ar RF induction plasma generated at atmospheric pressure [27–29]. Variation in particle size and morphology was reported from the synthesis of nano-sized particles of single-component oxides and binary oxide systems. Synthesized particles of

single-component oxides were spherical for $ZrO_2$, $Y_2O_3$, $Sm_2O_3$, $La_2O_3$, δ-$Al_2O_3$, $TiO_2$(atnatase), β-$Bi_2O_3$, and CuO; plate-like for $Nd_2O_3$, Cr2O3, and $Pr_2O_3$; polyhedral for $PrO_2$, $CeO_2$, and γ-$Fe_2O_3$; cubical for NiO, MgO, CaO, $Co_3O_4$, and $Mn_3O_4$; bar-like for $SnO_2$ and ZnO; and foil-like for β-PbO and $MoO_3$. In binary oxide systems, ($Cr_2O_3$, $Fe_2O_3$, $SnO_2$)–$Al_2O_3$, the distribution of component oxides was carefully investigated. For the $Cr_2O_3$–$Al_2O_3$ system, each component independently constituted its particles that were homogeneously distributed in the powder. With $Fe_2O_3$–$Al_2O_3$, the two components formed solid solutions. In $SnO_2$–$Al_2O_3$, the powders were composed of each component, where $SnO_2$ had a strong tendency to occupy the particle surface. For complex oxides, this technique was applied to the synthesis of nano-sized particles of perovskite-type oxides, $RFeO_3$(R: Eu, Yb), thin films of garnet-type oxides, $Y_3Al_5O_{12}$ and $Y_3Fe_5O_{12}$, barium ferrites, $Ba(Fe,Co,Ti)_{12}O_{19}$, barium hexaaluminate, $BaAl_{12}O_{19}$, and superconducting oxides of the Bi–Pb–Sr–Ca–Cu–O system [30–34].

For the synthesis of Ti-containing materials, titanium alkoxides were used as precursors because an appropriate water-soluble precursor was not available. As alkoxides are susceptible to water and even water vapor in air to undergo hydrolysis, a stabilizing reagent, tri-ethanol amine, was added to the liquid precursors [35–39]. Films of Ti-based materials, TiN, TiC, TiN–AlN, TiC–TiN, $Si_xN$–TiN, and Ti–Si–B–C systems, were prepared by injecting liquid precursors containing alkoxides and a stabilizing reagent. The procedure overcame the difficulty of processing by using water-sensitive alkoxides included below. In the synthesis of TaC nano-sized powders, a liquid precursor, tantalum ethoxide, was fed into Ar–$H_2$ RF induction plasma to form TaC through pyrolytic decomposition. As tantalum ethoxide is more reactive to water than titanium alkoxides, the liquid feeding system was set in an Ar-containing glove box [40].

Aqueous $TiCl_3$ solution was also used as a Ti source [41, 42]. Such a solution as a precursor is advantageous over widely used titanium(IV) compounds such as tetrachloride and alkoxides, in that it is stable under ambient conditions; thus, easily manipulated. The use of $TiCl_3$ led to the simultaneous incorporation of chlorine into the $TiO_2$ lattice, which exhibited enhanced photocatalytic properties and degraded luminescent properties.

## Size Control of Nanoparticles in Thermal Plasma Processing

Nano-scale size control of particles is crucial to the appearance of functions, in view of the quantum-size effects in catalytic, electric, magnetic, and optical properties. Also, narrowing the size distribution should contribute to the extension of the application area. The easiest and most effective way to synthesize uniform nano-sized particles is to allow chemical reactions to proceed under dilute conditions. On the contrary, practical process-control should be done under high precursor loading conditions.

The effects of processing parameters were investigated in the synthesis of $TiO_2$ nanoparticles via Ar/$O_2$ RF thermal plasma oxidation of liquid precursor mists [43]. Nucleation from a gas phase and the subsequent grain growth take place in the plasma tail. Therefore, size control should be done by modifying the temperature and flow distribution in the downstream of the plasma. We have demonstrated the particle size controlled synthesis of well-dispersed $TiO_2$ nanopowders via Ar/$O_2$ thermal plasma oxidation of liquid precursor mists through manipulating the cooling rates by injecting quench gases (Ar, He) [44]. In this case, the $TiO_2$ nanoparticles were synthesized via Ar/$O_2$ thermal plasma oxidation of atomized liquid precursors containing titanium tetrabutoxide (TTBO),

the titanium source, and diethanolamine, a chelate preventing the hydrolysis of TTBO. The RF power at a frequency of 2 MHz and power level of 25 kW was introduced to generate the plasma at a pressure of 53.3 kPa. The precursor was atomized into mists at the tip of the atomization probe, which was used to inject apatite suspensions for plasma-spraying coatings [45], by Ar carrier gas flowing through the probe.

Quench gas was injected two in different ways: transverse (Fig. 2a) and counter (Fig. 2b). Figure 2 compares the morphologies of the $TiO_2$ powders synthesized with and without Ar quench gas injections. X-ray diffractions showed that the synthesized powders consisted of rutile and anatase phases of $TiO_2$. The majority of particles were rounded, with sizes ranging from a few to about 200 nm. The plasma-generated particles showed weak agglomerations, which is in sharp contrast to those synthesized via most wet-chemical techniques.

The overall morphology of the powder does not alter significantly by injecting 100 l/min of Ar in the transverse mode (Fig. 3b), but the powder becomes appreciably finer by injecting the same amount of Ar in the counter flow mode (Fig. 3c), revealing the significance of the quenching method on powder properties. The size distributions of the powders were evaluated through an image analysis of photos taken using a scanning electron microscope (SEM). It was found that the powders synthesized without quench gas and with Ar transverse flow have similar median diameter, $d_{50}$, of $\sim$55 and 53 nm, respectively, while that made with Ar counter flow has a considerably smaller $d_{50}$ of $\sim$35 nm. In addition, the size distribution of the powder substantially narrowed by applying the counter flow Ar quench gas. The standard deviation $\sigma$ for the powders synthesized without quench gas was evaluated to be 22 nm. The Ar transverse flow increased $\sigma$ to 30 nm, while the Ar counter flow decreased $\sigma$ to 12 nm.

Modeling was conducted to better understand the effects of quench gases and optimize the process parameters and reactor design [44]. The plasma flow and temperature fields were simulated using a two-dimensional and turbulence fluid model. Since the particles are

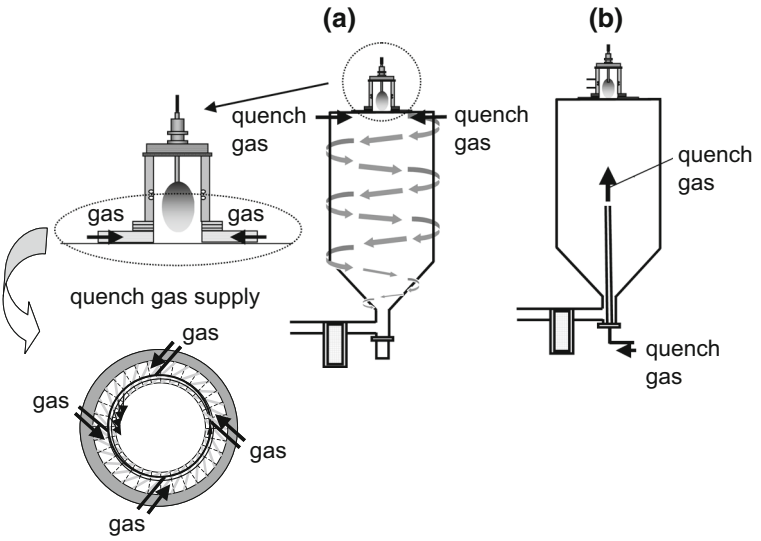


**Fig. 2** Experimental setups for **a** transverse swirl-flow injection and **b** counter-flow injection of quench gases [44]

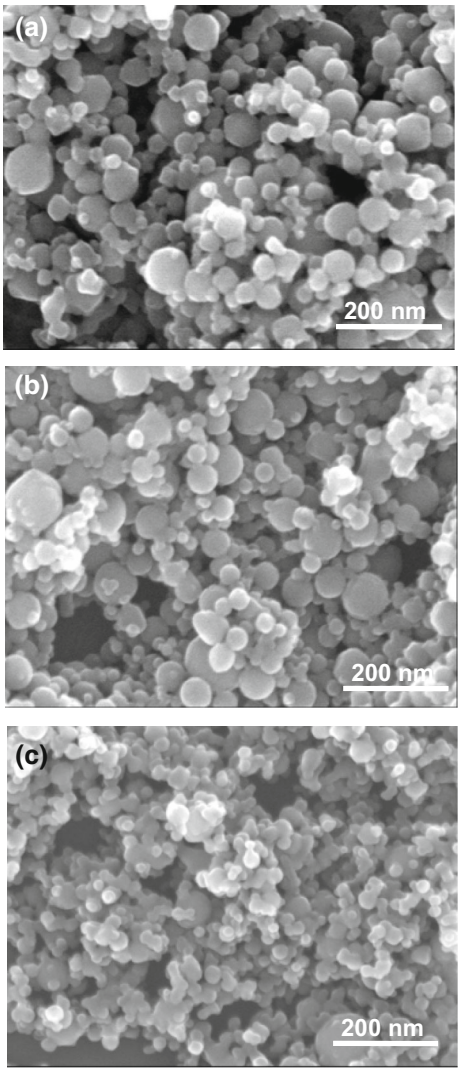


**Fig. 3** SEM micrographs showing morphologies of $TiO_2$ powders synthesized **a** without use of quench gas, **b** with transverse swirl-flow injection of 100 l/min of Ar, and **c** with counter-flow injection of 100 l/min of Ar [44]

synthesized from the vapor phase of the precursors, their trajectories should follow the streamlines of the fluid due to the small masses of the particles. As a simplified approach, the motion of a test particle with negligible mass and the infinite melting point in the plasma flow were traced. Figure 4 illustrates the calculated streamlines and temperature fields in the reactor. The dots in Fig. 4 indicate the predicted trajectories of a test particle released at the tip of the central probe. Comparing Fig. 4a, b, we can find that transversely injecting Ar does not significantly alter the temperature fields of the plasma and trajectories of the test particle. When Ar is injected counter to the plasma plume, however, it profoundly affects the temperature field and trajectories of particles (Fig. 4c). The greatly decreased size of the plasma plume allows the particle to remain for a shorter duration in the high temperature zone; hence, favoring finer particle formation. The above numerical analysis results support the experimental data given in Fig. 3.

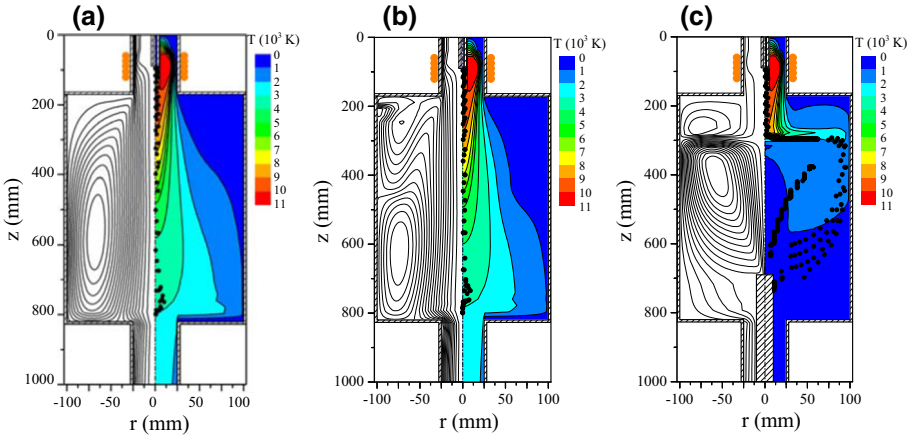


**Fig. 4** Streamlines and temperature distribution for: **a** no quench gas, **b** transverse swirl-flow injection of Ar at 100 slpm, and **c** counter flow injection of Ar at 100 slpm [44]

The effect of mass number of quenching gas was also observed in the synthesis of TaC nano-sized powder by injecting radially atomized mists of tantalum ethoxide into Ar-$H_2$ RF induction plasma at the bottom of the plasma torch [40]. The atomized precursor rapidly dissociated in the high-temperature region of the plasma flame and recombined as the temperature decreased. Nano-sized tantalum carbide was easily prepared, as shown in Fig. 5. The particle size decreased with the increase in the plasma cooling rate by injecting quenching gas into the tail flame. This technique can be used to decrease the temperature locally in the injected region and control the chemical reactions there. According to Soucy et al. [46], injecting Ar at 20 l/min should have an adequate cooling effect. However, the particles synthesized with the tail injection of Ar were not smaller than those synthesized when it was not injected. The broadening of size distribution shown in Fig. 6 indicates the turbulence of flow induced by the Ar gas radial injection. When He, which has a thermal conductivity higher than that of Ar, of small atomic weight was injected as the tail

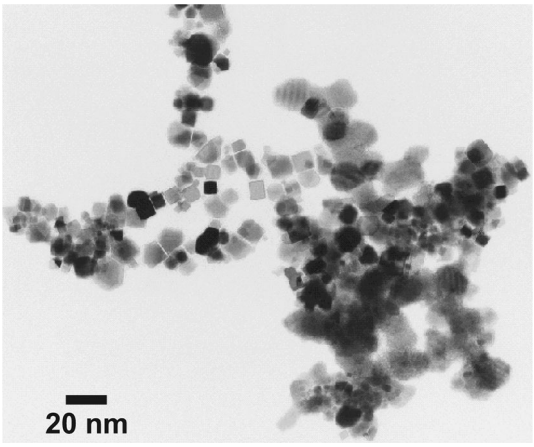


**Fig. 5** TEM image of plasma-synthesized TaC nano-sized particles [40]

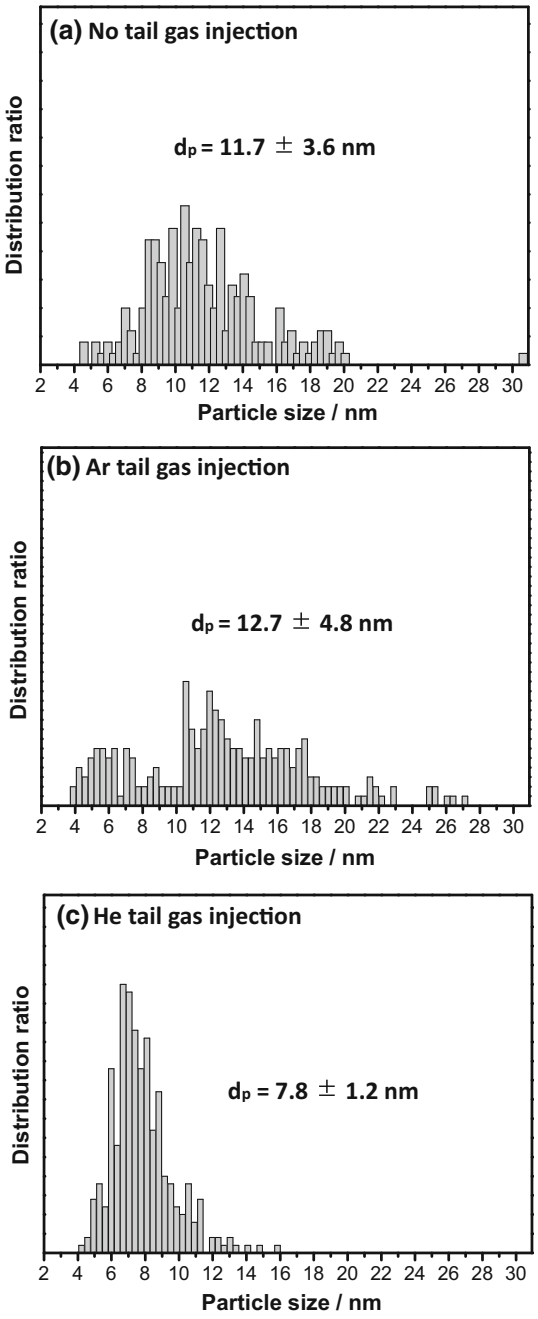


**Fig. 6** Size distributions of TaC nano-size particles synthesized with and without tail injection gases (pressure, 500 Torr). Number after ±is SD of particle size, $d_p$ [40]

quenching gas, the synthesized TaC particles were much smaller than those synthesized when no tail quenching gas was injected. The average size of the synthesized TaC nanoparticles decreased to 8 nm when He was injected at the plasma tail.

## Synthesis of Titanium Oxide Nanoparticles: Phase Selection and Formation of Non-equilibrium Chemical Composition

Non-equilibrium composition and structure were also observed in the nanoparticles as a result of rapid cooling at the plasma tail flame and are extremely interesting phenomena from the scientific viewpoint.

Titanium dioxide, which has classically been used as a white pigment, exhibits interesting properties, such as high transparency in the visible wavelength region, high refractive index, and remarkable chemical and thermal stabilities, allowing it to be applied in photocatalysis, solar cells, semiconducting gas sensors, bio sensors, electronic and magneto-electronic devices, and as a building block for photonic crystals.

Titanium dioxide is known to have two common polymorphs: anatase and rutile. Interestingly, thermodynamically metastable anatase predominates undoped $TiO_2$ nanopowders, which can be explained from a kinetic viewpoint based on classical homogeneous nucleation theory [47, 48], while decreasing the oxygen partial pressure in the vapor phase resulted in pure rutile nanoparticles [49].

The nucleation of rutile and anatase from $TiO_2$ melt was analyzed by thermodynamic calculation using estimated values of the interfacial energy between the liquid and solid phases in the pure $TiO_2$ system [47]. Based on classic homogeneous nucleation theory, estimated interfacial energies were used to evaluate critical nucleation energies for homogeneous nucleation in melt. Figure 7 shows the temperature dependence of the ratio $\Delta G_{\text{rutile}}^*/\Delta G_{\text{anatase}}^*$, where $\Delta G_{\text{rutile}}^*$ and $\Delta G_{\text{anatase}}^*$ are the critical free energies for stoichiometric rutile and anatase $TiO_2$, respectively. It can be seen that the value of $\Delta G_{\text{rutile}}^*/\Delta G_{\text{anatase}}^*$ is greater than unity over a wide range of temperatures, indicating that metastable anatase $TiO_2$ nucleates preferentially. This phase formation behavior agrees with the experimental observation that, under a high cooling rate, anatase solidifies from the melt directly in high-temperature syntheses with a high degree of undercooling, while rutile solidifies at a temperature close to the melting point of $TiO_2$.

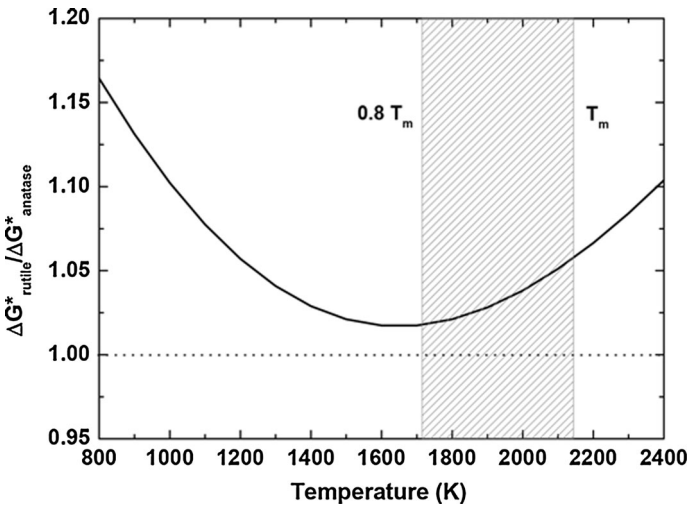


**Fig. 7** Temperature dependence of critical free energy ratio, $\Delta G_{\text{rutile}}^*/\Delta G_{\text{anatase}}^*$, where $\Delta G_{\text{rutile}}^*$ and $\Delta G_{\text{anatase}}^*$ are critical free energies for stoichiometric rutile and anatase $TiO_2$, respectively [48]

The structural characteristics in the two $TiO_2$ phase are apparently related to the formation of the defective rutile structure (with an oxygen deficiency) that forms from doping of metal ions with lower valence than $Ti^{4+}$ or under reduced conditions, which alter the densely arranged lattice plane in the tetragonal structure of the crystals. The tolerance of anatase and rutile against the presence of defects can be qualitatively correlated with the local environment of titanium in anatase and rutile. In both structures, Ti is sixfold-coordinated, but the number of shared octahedral edges increases from two in rutile to four in anatase. Traditional crystal chemical theory argues that shared edges should lead to cation–cation repulsion and structural destabilization, in accordance with the relative stability of both phases. Rutile has greater tolerance than anatase toward oxygen vacancies due to fewer shared edges in the crystal structure of rutile. Substitution of $Ti^{4+}$ in $TiO_2$ with trivalent ions or divalent ions, such as like $Fe^{3+}$ and $Co^{2+}$, introduces oxygen vacancies to maintain charge neutrality. Synthesis of $TiO_2$ under reduced atmosphere also gives rise to the formation of oxygen vacancies. Therefore, rutile $TiO_2$ is preferentially formed [48, 49].

The next key point in this chapter is the use of liquid mixtures, in which some metal elements exist as ions in aqueous solutions or as constituent atoms of metallorganic compounds. The use of liquid precursors enables uniform nanoparticles to be formed and has the advantages of high production rate. Precise control of chemical composition also provides the opportunity to obtain particles of non-equilibrium doping, in which the doping quantity is larger than the solubility limit under equilibrium condition.

Doped $TiO_2$ nanoparticles have been synthesized via $Ar/O_2$ thermal plasma oxidation of atomized liquid precursors. In the case of iron doping, mixtures of TTBO and ferrocene dissolved in ethanol were used as precursors [48]. The liquid precursor for uropium doping was made in the following procedure [50]. Titanium tetraisobutoxide was added to diethanolamine to stabilize the TTBO against hydrolysis. Separately, uropium nitrate and citric acid were dissolved in water, and the pH of the solution was adjusted to 9.0 with ammonia solution. Mixing the above two solutions yields a stable clear solution to be used as the liquid precursor. For $Er^{3+}$ and $Co^{2+}$ doping, the same procedure as $Co^{2+}$ doping was used to prepare clear liquid solution without any precipitate [51, 52].

In iron-doped $TiO_2$ nanoparticles, no other phases except anatase and rutile $TiO_2$ were identified for a wide range of iron to titanium atomic ratios ($R_{Fe/Ti}$) ranging from 0 to 0.2, though the solubility of iron in $TiO_2$ was reported to be around 5 at.% by conventional wet processes [48]. Iron doping strongly promoted the formation of rutile because rutile is more tolerant than anatase against defects such as oxygen vacancies resulting from the substitution of $Fe^{3+}$ for $Ti^{4+}$ in $TiO_2$. The concentration of oxygen vacancies reached its maximum at $R_{Fe/Ti} = 2\%$, above which the excessive oxygen vacancies tended to concentrate. As a result of this clustering, an extended defect, such as crystallographic shear structure, was established (Fig. 8). The highly iron-doped $TiO_2$ nanocrystals showed paramagnetic properties, as $Fe^{3+}$ substitutes $Ti^{4+}$ and is uniformly distributed in the $TiO_2$ lattice [53].

The solubility of $Co^{2+}$ in the $TiO_2$ lattice was determined to be around 2.0 at.% [52]. The solubility limit is substantially smaller than that ($\sim$20 at.%) for $Fe^{3+}$ in $TiO_2$, which might be understood by considering the following facts. (1) For sixfold coordination, $Co^{2+}$ (0.0745 nm, high spin state) is much larger than $Fe^{3+}$ (0.0645 nm, high spin state), whereas the later has an ionic size close to that of $Ti^{4+}$ (0.0605 nm). (2) Every two $Fe^{3+}$ ions, while only one $Co^{2+}$, are needed to create one oxygen vacancy for charge compensation; hence, within the tolerance of the $TiO_2$ lattice, the amount of $Co^{2+}$ that can be accommodated into $TiO_2$ is smaller. (3) Cobalt oxide is more alkaline than its iron counterpart from the Lewis definition of acid and base; therefore, cobalt oxide is more

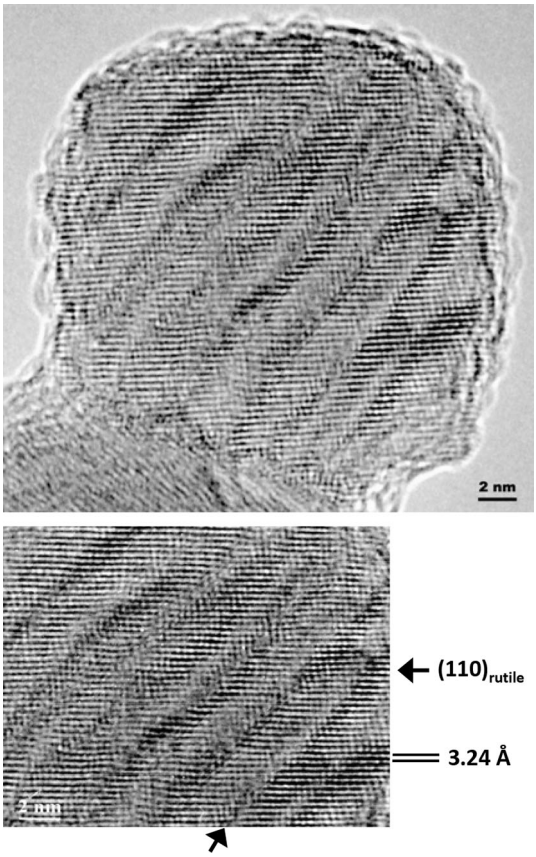


**Fig. 8** HRTEM images of highly iron-doped nanopowder with $R_{Fe/Ti} = 0.2$. d spacing of 0.324 nm corresponds to rutile {1 1 0} planes [48]

readily able to form compounds ($CoTiO_3$, $Co_2TiO_4$) with $TiO_2$, instead of $Co^{2+}$ incorporation into $TiO_2$ via $Ti^{4+}$ substitution by $Co^{2+}$.

The amount of $Eu^{3+}$ that can be doped into the $TiO_2$ lattice was limited up to 0.5 at.%, above which $Eu_2Ti_2O_7$ pyrochlore was formed. Such a phenomenon is conceivable from the quite large size discrepancy between $Ti^{4+}$ (0.0605 nm for sixfold coordination) and $Eu^{3+}$ (0.0947 nm for sixfold coordination) ions. Figure 9 illustrates typical emission spectra of $TiO_2$:$Eu^{3+}$ nanoparticles as well as those of pure $Eu_2O_3$ and $Eu_2Ti_2O_7$ under 325-nm He-Cd laser excitation [50]. It is the $^5D_0 \rightarrow {}^7F_2$ transition that gives a sharp red emission peak. The $Eu^{3+}$-doped samples exhibit emissions clearly different from those of $Eu_2O_3$ and $Eu_2Ti_2O_7$, in terms of peak positions and peak shapes, implying different local environments. Efficient non-radiative energy transfer from the $TiO_2$ host to $Eu^{3+}$ ions, which was seldom reported in the wet-chemically derived nanoparticles or thin films of the same system, was confirmed by combined studies of excitation, UV–Vis absoption, and photoluminescence (PL) spectroscopy. Single-particle fluorescence spectroscopy was also used to investigate the defect-mediated PL dynamics of $Eu^{3+}$-doped $TiO_2$ nanoparticles [54]. The PL spectra and time traces of individual nanoparticles or aggregates revealed that the PL band originating from defects at the $TiO_2$ surface appears in the visible region. Energy transfer from defects to surface-located $Eu^{3+}$ ions is experimentally suggested.

Highly crystalline, highly luminescent nanopowders of $Er^{3+}$-doped $TiO_2$ have been also synthesized [51]. Results were similar to those for the $Eu^{3+}$-doped $TiO_2$. The large size

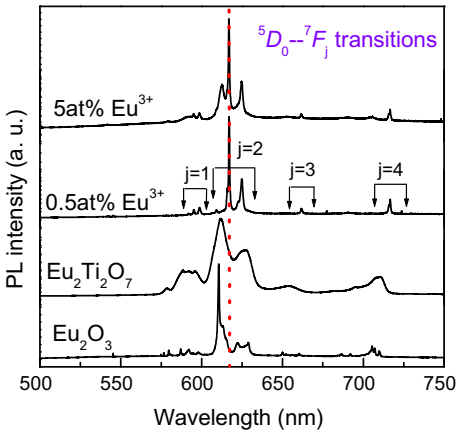


**Fig. 9** Emission spectra of $Eu^{3+}$-doped $TiO_2$ nanopowders compared with those of $Eu_2O_3$ and $Eu_2Ti_2O_7$ [50]

mismatch between $Ti^{4+}$ (0.065 nm) and $Er^{3+}$ (0.089 nm) made it difficult for $Er^{3+}$ to enter the $TiO_2$ lattice. Approximately 0.5 at.% of $Er^{3+}$ could be doped into the $TiO_2$ lattice, above which $Er_2Ti_2O_7$ pyrochlore appeared as an impurity phase. Bright PL at $\sim$1.53 μm was observed from the nanopowders either by directly exciting the $Er^{3+}$ activator or exciting the $TiO_2$ host lattice. A comparative study showed that the nanopowder of the same system made using a wet-chemical coprecipitation method did not show bright PL due to the lack of energy transfer from the $TiO_2$ host to $Er^{3+}$ activators.

High-concentration niobium (V)-doped $TiO_2$ nanoparticles of non-equilibrium chemical composition have been synthesized with various $Nb^{5+}$ concentrations (Nb/(Ti + Nb) = 0–25.0 at.%), in which niobium pentaethoxide was used as a niobium source [55]. Solubility as high as $\sim$25.0 at.% has not been achieved with wet-chemical techniques. The preferable anatase formation was attained in the plasma-synthesized powders and enhanced by niobium doping. All the powders were heated at high temperatures (600–800°C) to investigate their phase transformation, band gap variation, inter-particulate binding behavior, and photocatalytic stability. The transformation from anatase to rutile was effectively inhibited by increasing the $Nb^{5+}$ content. The $Nb^{5+}$ doping prevented the band gap of $TiO_2$ from narrowing after heating. At high temperatures, $Nb^{5+}$ doping could not only preserve particle size but also prevent inter-particulate binding.

In ($Eu^{3+}$–$Nb^{5+}$)-co-doped $TiO_2$ nanopowders, doping $Nb^{5+}$ cannot have an appreciable effect on $Eu^{3+}$ solubility (0.5 at. %) in the $TiO_2$ host lattice, but can significantly inhibit the increase in the rutile weight fraction for $TiO_2$. The 617-nm PL intensity at 350-nm indirect excitation through energy transfer is considerably weaker than that at 467-nm direct excitation, indicating that a defect state level in the $TiO_2$ host lattice might be lowered below the excited state of $Eu^{3+}$ by doping $Nb^{5+}$, which is conceivable from a relatively large amount of oxygen deficiencies yielded in the $TiO_2$ host lattice [56].

## Photocatalystic Properties Of Nano-sized Titanium Oxide Particles Doped with Transition Metals

Since the discovery of the Honda–Fujishima effect in 1972 [57], semiconductor photocatalysts have drawn enormous attention due to their potential application in water and air purification, anti-virus, deodorizing, self-cleaning, as well as photocatalytic hydrogen

generation and $CO_2$ reduction. Although different types of photocatalysts have been developed over the past 40 years, $TiO_2$ is still regarded as the most promising due to its high chemical stability, low toxicity, and suitable band position. However, $TiO_2$ can only respond to UV light, which greatly inhibits its utilization under visible light. Therefore, significant efforts have been made to make $TiO_2$ exhibit activity under visible light, such as doping and noble metal supporting.

Well-crystallized iron(III)-doped $TiO_2$ nano-size powders with controlled doping concentration and uniform dopant distribution prepared using a thermal plasma method were applied to photocatalytic measurement [58]. The photocatalytic reactivity of as-synthesized $TiO_2$ nanopowders with iron doping concentration ($R_{Fe/(Fe+Ti)}$) up to 16.4 at.% was quantified in terms of the degradation rates of methyl orange (MO) in aqueous $TiO_2$ suspension under UV and visible light irradiation. The doping concentration was larger than that at the optimal iron doping concentration under UV irradiation; therefore, the nominally undoped $TiO_2$ had the highest photocatalytic reactivity, suggesting that iron doping in $TiO_2$ with a particle size of 50–70 nm is detrimental. Under visible light irradiation, however, $TiO_2$ with an intermediate iron doping concentration at $\sim$1 at.% had the highest photocatalytic reactivity due to the narrowing of the band gap so that it could effectively absorb the light with longer wavelengths. This suggests that iron doping with an optimal concentration holds promise for finding photocatalysts that are active in the visible light region.

The photocatalytic properties of $TiO_2$-based nano-size powders were further evaluated: Nb-doped [55], Nb- and Fe-codoped [59], Nb- and Eu-codoped [60], and Cl-doped [41] $TiO_2$. The properties were discussed in terms of defect chemistry to understand what effect oxygen defects have on photocatalytic performance and extend the potential applications of $TiO_2$ as a photocatalyst into the visible light region. More interestingly, Nb- and Eu-codoped powder exhibited improved photocatalytic performance under visible light illumination with the 600–700-nm wavelength range, which is relatively long in visible light wavelength range (400–700 nm) [60].

## Phase Formation in Other Nano-sized Oxide Particles Composed of Three Metal Elements

Cubic-structured $Y_2O_3$:$Eu^{3+}$ solid solutions (optimal $Eu^{3+}$ content: $\sim$5 at.%) exhibit sharp red emissions at $\sim$610 nm arising from the $_5D^0$–$_7F^2$ electronic transition of $Eu^{3+}$. The material is currently the most widely used red phosphor for frequent applications in areas such as fluorescent lamps, white LEDs, plasma display panels, flat-panel displays, field emission displays, and cathode-ray tubes. The $Y_2O_3$:$Eu^{3+}$ phosphors are classically made via solid state reaction at $\sim$1500 °C and are usually characterized by large particle size (up to tens of μm), irregular particle shape, and significant aggregation. Current advances in higher solution displays, however, require finer phosphors of better dispersion to improve resolution by decreasing pixel size. Yttrium oxide, $Y_2O_3$, is generally cubic structured under ambient conditions, but will transform into a monoclinic polymorph upon being heated to close to its melting point ($\sim$2430 °C). The monoclinic polymorph of $Y_2O_3$ is nonetheless frequently observed in nanopowders made via flame pyrolysis, and Skandan et al. argued that this is due to a ‘‘size effect’’, i.e., the very tight curvature of the nanoparticles can increase the internal pressure ($\Delta P = 2\sigma/r$, s: surface energy and r: radius of particle) within the particle [61]. In flame pyrolysis and in thermal plasma processing,

particles are formed via nucleation/growth through gas–solid and/or gas–liquid–solid processes. Upon cooling of the species generated at a high temperature close to or above the melting point of $Y_2O_3$, the monoclinic polymorph would nucleate with priority then quenched to the final product by subsequent rapid cooling.

Well-dispersed ultrafine particles of $Y_2O_3$:Eu were synthesized in one step via RF thermal plasma oxidation of atomized alcohol solutions of the component nitrates [62]. Powders collected at the reactor wall and filter were examined by X-ray diffractometry (XRD). The powders of pure$Y_2O_3$, collected from either the reactor wall (Fig. 10, line a) or filter (Fig. 10, lineb), are mixtures of the monoclinic and cubic phases. For pure $Y_2O_3$, the powders from the reactor wall and filter have ~54.8 and ~44.5 wt% of the monoclinic phase, respectively. Doping with only 5at % of $Eu^{3+}$ raised the monoclinic content to ~63 wt% (Fig. 10, line c) while codoping with 20 at.% of $Sc^{3+}$ (relative to total cations) turned the product into an almost pure cubic phase (monoclinic content: ~10 wt%, Fig. 10, line d). The enhanced monoclinic crystallization by $Eu^{3+}$ doping arises from the much lower temperature of the cubic-monoclinic phase transition of $Eu_2O_3$ (~1100 °C under atmospheric pressure and ~900 °C under 2.5 GPa). The low transition temperature allows the monoclinic polymorph to be stable over a much wider temperature range; thus, enhanced nucleation of the monoclinic phase can be expected. The significantly suppressed monoclinic crystallization by $Sc^{3+}$ codoping is due to the fact that $Sc_2O_3$ (melting point ~2400 °C) has no reported cubic → monoclinic phase transition; thus, its presence retards monoclinic nucleation and stabilizes the cubic phase at the same time. Shifting of the C(440) diffractions (Fig. 10) to the lower-angle side by $Eu^{3+}$ doping (lattice expansion) and to the higher angle side by $Sc^{3+}$ codoping (lattice contraction) suggests the direct

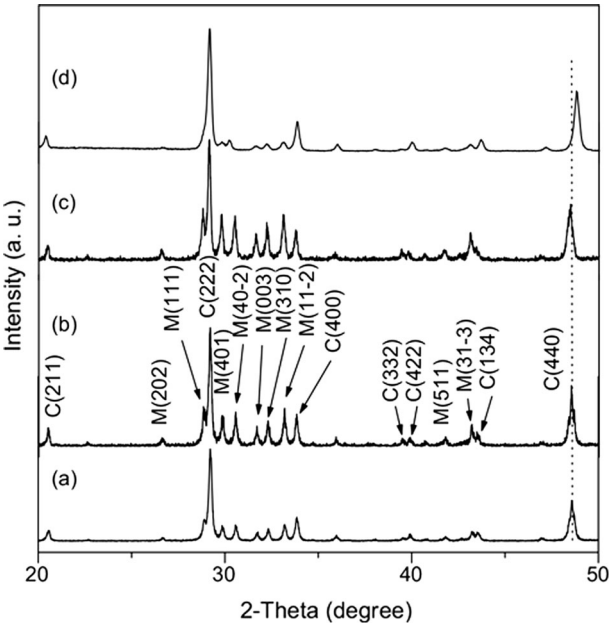


**Fig. 10** XRD patterns of oxidation products with nominal compositions of **a** pure$Y_2O_3$ collected from reactor wall and **b** pure$Y_2O_3$, **c** $(Y_{0.95}Eu_{0.05})_2O_3$, and **d** $[(Y_{0.8}Sc_{0.2})_{0.95}Eu_{0.05}]_2O_3$ collected from filter. ''M'' and ''C'' denote monoclinic and cubic structured phases, respectively [62]

formation of solid solutions, and the shifting is understandable from the differing ionic sizes of $Y^{3+}$ (0.0900 nm), $Sc^{3+}$ (0.0745 nm), and $Eu^{3+}$ (0.0947 nm).

Barium titanate exhibits excellent dielectric properties such as high dielectric constant, small dielectric loss, low leakage current, and high dielectric breakdown strength. It has a wide range of applications in electronic and electro-optic devices, such as thermistors, multilayer ceramic capacitors (MLCC), microwave absorbers, and transducers. The progress in electronic technologies has led to a demand for MLCCs of higher density and capacity, but to fabricate them, we need finer BaTiO3 powders with particle sizes of below 50 nm. Barium titanate is used in combination with special additives ($Sr^{2+}$) that modify and enhance its dielectric properties. It is a ferroelectric perovskite, while $SrTiO_3$ is a quantum paraelectric material. The Curie temperature can be adjusted by varying the Ba/(Ba + Sr) ratio. Barium titanate is noncentrosymmetric tetragonal, and adding Sr changes it into a centrosymmetric cubic phase. The properties of barium strontium titanate ((Ba, Sr)$TiO_3$) are usually dependent on the particle size, purity, dispersability, and homogeneity of powders.

Barium strontium titanate nano-sized powders were synthesized via spray pyrolysis of a liquid precursor mist [63]. To adjust the cation stoichiometry of the complex oxide, liquid precursors were prepared by mixing titanium butoxide stabilized with diethanolamine and aqueous solutions of barium nitrate and strontium nitrate stabilized with citric acid. The molar ratios of titanium, barium, and strontium ions (Ba/(Ba + Sr) and (Ba + Sr)/Ti ratios) in the liquid precursor were varied. Changing the metallic ratio in the liquid precursors had a strong effect on the formation of impurity $BaCO_3$ and $Ba_2TiO_4$ phases. Figure 11 shows the XRD patterns of (Ba, Sr)$TiO_3$ with Ba/(Ba + Sr) ratios from 0.0 to 1.0, in which almost no diffraction from impurities was observed. The Ba/(Ba + Sr) ratio was varied to prepare impurity-free powders at 0.7, 0.8, and 0.9 with the (Ba + Sr)/Ti ratios of 0.98, 0.98, and 0.97, respectively. The peak positions of (Ba, Sr)$TiO_3$ shifted as a

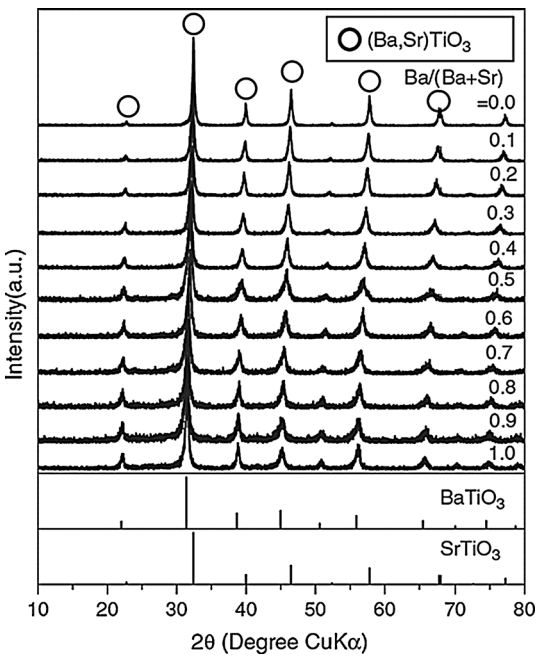


**Fig. 11** Variation in XRD patterns of (Ba, Sr)$TiO_3$ powders made by plasma pyrolysis of liquid precursor with Ba/(Ba + Sr) ratio of precursors. (Ba(Ba + Sr) = 0.0–0.6 of (Ba + Sr)/Ti = 1.00), (Ba/(Ba + Sr) = 0.7–0.8 of (Ba + Sr)/Ti = 0.98), (Ba/(Ba + Sr) = 0.9 of (Ba + Sr)/Ti = 0.97), and (Ba/(Ba + Sr) = 1.00 of (Ba + Sr)/Ti = 1.00) [63]

result of changing the Ba/(Ba + Sr) ratio in the liquid precursor. The increase in lattice spacing from $SrTiO_3$ to $BaTiO_3$ can be explained on the basis of the ionic radius of the two cations. $Ba^{2+}$ (0.161 nm) has a larger radius than $Sr^{2+}$ (0.140 nm); hence, substitution of $Ba^{2+}$ for $Sr^{2+}$ will surely enlarge the lattice.

## Highly Dispersed Behavior of Thermal Plasma-Synthesized Nanoparticles in Liquid Media

Nanopowders agglomerate more strongly than submicrometer powders, and some of the particles coagulate strongly. Agglomerated nanoparticles do not fragment easily and are difficult to disperse perfectly. Therefore, easily dispersive nanoparticles are needed to extend the application area of nano-size powders. Spherical $TiO_2$ nanoparticles, with mean primary particle sizes of 29 and 53 nm, denoted as Plasma A and B powders, respectively, were synthesized in $Ar/O_2$ RF induction thermal plasma pyrolysis of atomized liquid precursors containing titanium tetrabutoxide [44]. The plasma-synthesized nanoparticles at 1.0 vol% in solid fraction were dispersed by ultrasonic irradiation in the aqueous solution of polyacrylic acid [64]. Figure 12 shows transmission electron microscope (TEM) images of the particles of Plasma A and B powders and of the commercial P25 powder. Nanoparticles were taken from each suspension, which had all been ultrasonically irradiated, and put on a carbon grid. Particles aggregated automatically as they dried, and the commercial P25 powder showed the strongest coagulation among the primary particles (Fig. 12c). However, the particles of Plasma A and B powders did not appear to have coagulated very much (Fig. 13a, b). The mean aggregate size of the plasma-synthesized powders in aqueous suspension measured using a particle size analyzer corresponded exactly to the mean primary particle size evaluated by examining surface area data and analyzing SEM images, which suggests that the plasma-synthesized $TiO_2$ nanoparticles were individually dispersed in water [65].

## Future Perspective on Applications of Functional Nanoparticles Prepared by Thermal Plasma Processing

When aiming at the application of highly functional nanoparticles, it is considered necessary to structure nanoparticles in the form of (1) dispersoids, (2) fillers, and (3) patterns. For example, in the case of red, green, and blue fluorescent particles used in plasma displays, fluorescent particles of several micrometers in diameter produced using a solid-phase method by comminution are currently used. However, when using even smaller fluorescent nanoparticles of several tens of nm with excellent dispersion, the resolution markedly improves and light scattering decreases, as a result, high energy efficiency can be expected. Similarly, the absorption properties of GHz and electromagnetic wave absorbers used in mobile devices are significantly improved with the use of magnetic nanoparticles completely dispersed in plastic matrices. Consequently, whether using the liquid phase or vapor method for synthesis, the most important tasks at present are to improve the crystallinity of nanoparticles, create additional functions through composition control, prevent aggregation through surface property control, and prepare complete dispersoids. In situ dispersion is expected to become key, regardless of the synthesis method used. In thermal plasma processing, nanoparticles are formed through coagulation from the vapor phase.

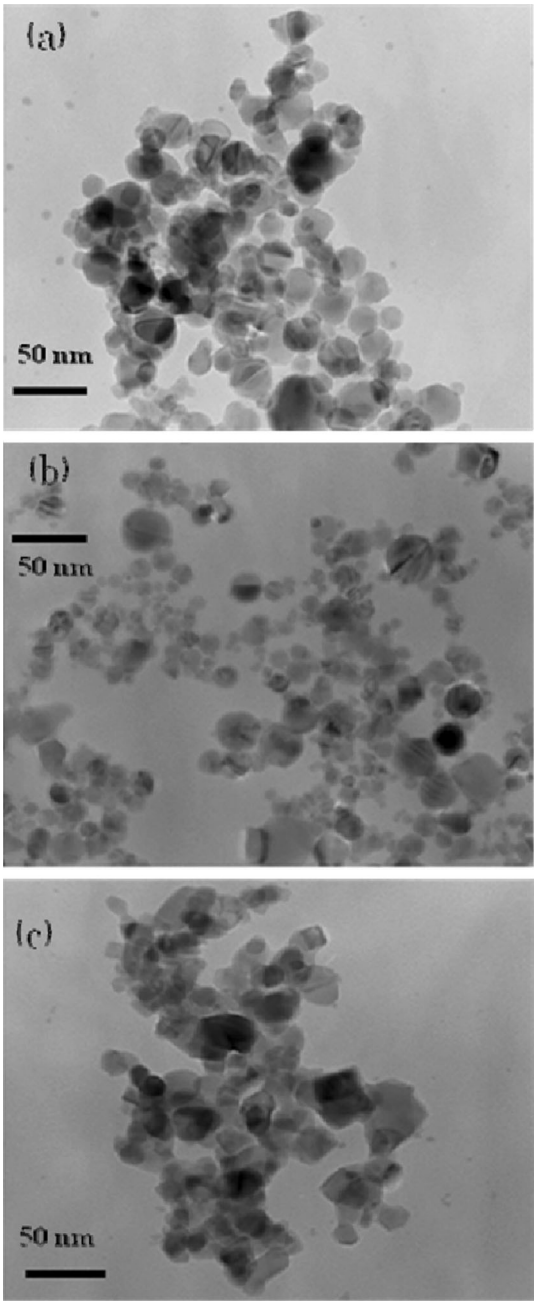


**Fig. 12** TEM images of $TiO_2$ nanoparticles taken from suspensions of **a** plasma B **b** plasma A, and **c** P25 powders [65]

The thermal plasma method, although similar to the spray-pyrolysis and flame-spray methods, can produce highly crystalline nanoparticles with little surface residue since the synthesis temperature is far higher. Because high crystallinity is related to functionalization, and the surface control is indispensable to dispersion, thermal plasma processing is

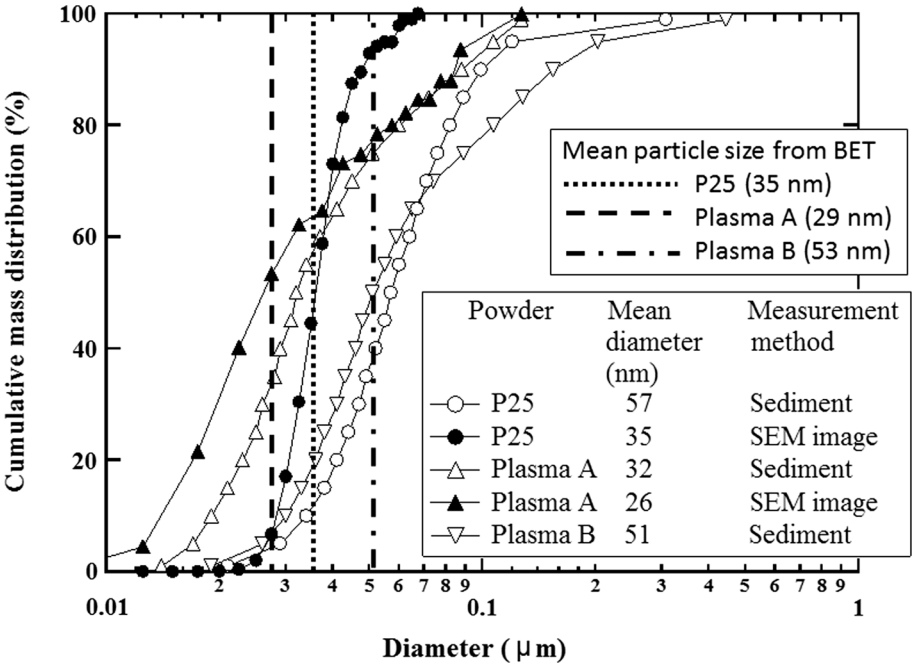


**Fig. 13** Aggregate size of $TiO_2$ nanoparticles in aqueous suspension. "Sediment" under "measurement method" denotes measurement using X-ray particle size analyzer. "SEM image" denotes measurement by analyzing SEM images. "Mean particle size from BET" denotes measurement from surface area and powder density data [65]

expected to make a significant contribution to nanoparticle applications. In fact, plasma-synthesized nanoparticles are spherical and hardly agglomerated, and through an appropriate dispersion procedure, particles are individually dispersed in water. We expect the possible synthesis of functional nanoparticles, whose prominent functions can be given only by thermal plasma processing.

## References

1. Schmid G (ed) (2004) Nanoparticles—from theory to application. WILEY-VCH Verlag GmbH & Co. KGaA, Berlin
2. Boulos MI, Fauchais P, Phender E (1994) Thermal plasmas: fundamental and applications, vol 1. Plenums Press, New York
3. Young RM, Phender E (1985) Generation and behavior of fine particles in thermal plasmas—a review. Plasma Chem Plasma Process 5(1):1–37. doi:10.1007/BF00567907
4. Li YL, Ishigaki T (2001) Spheroidization of titanium carbide powders by induction thermal plasma processing. J Am Ceram Soc 84(9):1929–1936. doi:10.1111/j.1151-2916.2001.tb00939.x
5. Boulos MI (1992) RF induction plasma spraying: state-of-the-art review. J Therm Spray Technol 1(1):33–40. doi:10.1007/BF02657015
6. Kong P, Huang TT, Pfender E (1986) Synthesis of ultrafine silicon-carbide powders in thermal arc plasmas. IEEE Trans Plasma Sci 14(4):357–369. doi:10.1109/TPS.1986.4316563
7. Kong PC, Pfender E (1987) Formation of ultrafine beta-silicon carbide powders in an argon thermal plasma-jet. Langmuir 3(2):259–265. doi:10.1021/la00074a020

8. Chang Y, Kong PC, Pfender E (1989) Characterization of silicon-nitride particles synthesized in an atmospheric-pressure convection-stabilized arc. Plasma Chem Plasma Process 9(1):73–93. doi:10.1007/BF01015827
9. Chang Y, Young RM, Pfender E (1989) Silicon-nitride synthesis in an atmospheric-pressure convection-stabilized arc. Plasma Chem Plasma Process 9(2):277–289. doi:10.1007/BF01054286
10. Tamou Y, Yoshida T, Akashi K (1987) The synthesis of ultrafine silicon carbide in a hybrid plasma. J Jpn Inst Met 51(8):737–742
11. Lee HJ, Eguchi K, Yoshida T (1990) Preparation of ultrafine silicon-nitride, and silicon-nitride and silicon-carbide mixed powders in a hybrid plasma. J Am Ceram Soc 73(11):3356–3362. doi:10.1111/j.1151-2916.1990.tb06461.x
12. Kijima K, Noguchi H, Konishi M (1989) Sintering of ultrafine SiC powders prepared by plasma CVD. J Mater Sci 24(8):2929–2933. doi:10.1007/BF02385649
13. Guo JY, Gitzhofer F, Boulos MI (1995) Induction plasma synthesis of ultrafine SiC powders from silicon and CH4. J Mater Sci 30(22):5589–5599. doi:10.1007/BF00356691
14. Guo JY, Gitzhofer F, Boulos MI (1997) Effects of process parameters on ultrafine SiC synthesis using induction plasma. CH4. J Mater Sci 17(2):219–249. doi:10.1007/BF02766817
15. Soucy G, Jurewicz JW, Boulos MI (1995) Parametric study of the plasma synthesis of ultrafine silicon-nitride powders. J Mater Sci 30(8):2008–2018. doi:10.1007/BF00353026
16. Rao NP, Tymiak N, Blum J, Neuman A, Lee HJ, Girshick SL, McMurry PH, Heberlein J (1998) Hypersonic plasma particle deposition of nanostructured silicon and silicon carbide. J Aerosol Sci 29(5/6):707–720. doi:10.1016/S0021-8502(97)10015-5
17. Pratsinis SE, Vemury S (1996) Particle formation in gases: a review. Powder Technol 88(3):267–273. doi:10.1016/S0032-5910(96)03130-0
18. Pratsinis SE (1998) Flame aerosol synthesis of ceramic powders. Prog Energy Combust Sci 24(3):197–219. doi:10.1016/S0360-1285(97)00028-2
19. Vemury S, Pratsinis SE (1995) Dopants in flame synthesis of titania. J Am Ceram Soc 78(11):2984–2992. doi:10.1111/j.1151-2916.1995.tb09074.x
20. Hinklin T, Toury B, Gervais C, Babonneau F, Gislason JJ, Morton RW, Laine RM (2004) Liquid-feed flame spray pyrolysis of metalloorganic and inorganic alumina sources in the production of nanoalumina powders. Chem Mater 16(1):21–30. doi:10.1021/cm021782t
21. Laine RM, Marchal JC, Sun HP, Pan XQ (2006) Nano-α-$Al_2O_3$ by liquid-feed flame spray pyrolysis. Nat Mater 5(9):710–712. doi:10.1038/nmat1711
22. Li YL, Ishigaki T (2001) Synthesis of crystalline micron spheres of titanium dioxide by thermal plasma oxidation of titanium carbide. Chem Mater 13(5):1577–1584. doi:10.1021/cm000893u
23. Ishigaki T, Li YL, Kataoka E (2003) Phase formation and microstructure of titanium oxides and composites produced by thermal plasma oxidation of titanium carbide. J Am Ceram Soc 86(9):1456–1463. doi:10.1111/j.1151-2916.2003.tb03496.x
24. Oh SM, Li JG, Ishigaki T (2005) Nanocrystalline $TiO_2$ powders synthesized by in-flight oxidation of TiN in thermal plasma: mechanisms of phase selection and particle morphology evolution. J Mater Res 20(2):529–537. doi:10.1557/JMR.2005.0070
25. Akhtar MK, Pratsinis SE, Mastrangelo SVR (1994) Vapor phase synthesis of Al-doped titania powders. J Mater Res 9(5):1241–1249. doi:10.1557/JMR.1994.1241
26. Lee JE, Oh SM, Park DW (2004) Synthesis of nano-sized Al doped $TiO_2$ powders using thermal plasma. Thin Solid Films 457(1):230–234. doi:10.1016/j.tsf.2003.12.027
27. Kagawa M, Ohta H, Komatsu H, Syono Y (1985) Precipitation of γ-$Fe_2O_3$ from ultrahigh temperature plasma. Jpn J Appl Phys 24(4):477–481. doi:10.1143/JJAP.24.477
28. Suzuki M, Kagawa M, Syono Y, Hirai T (1992) Synthesis of ultrafine single-component oxide particles by the spray-ICP technique. J Mater Sci 27(3):679–684. doi:10.1007/BF02403879
29. Kato Y, Kagawa M, Syono Y (1998) Component distribution in plasma-deposited ultrafine powders of binary ($Cr_2O_3$, $Fe_2O_3$, $SnO_2$)–$Al_2O_3$ systems. Mater Lett 35(3–4):266–269. doi:10.1016/S0167-577X(97)00261-9
30. Mizoguchi Y, Onodera H, Yamauchi H, Kagawa M, Syono Y, Hirai T (1991) Mössbauer spectra and magnetic susceptibilities of ultrafine hexagonal $RFeO_3$(R: Eu, Yb) particles formed by the spray inductive coupled plasma technique. Mater Sci Eng, A 217:164–166. doi:10.1016/S0921-5093(96)10339-7
31. Mizoguchi Y, Kagawa M, Syono Y, Hirai T (2001) Film synthesis of $Y_3Al_5O_{12}$ and $Y_3Fe_5O_{12}$ by the spray-inductively coupled plasma technique. J Am Ceram Soc 84(3):651–653. doi:10.1111/j.1151-2916.2001.tb00717.x
32. Mizoguchi Y, Kagawa M, Syono Y, Hirai T (1996) $Ba(Fe_{12-x}Co_xTi_x)_{12}O_{19}$ (x = 0, 0.6, 0.9) films synthesized by the spray-ICP technique. Mater Trans, JIM 37(5):1177–1181

33. Uzawa M, Kagawa M, Syono Y (1993) Synthesis of barium hexaaluminate by the spray-ICP technique. Mater Lett 17(3–4):187–189. doi:10.1016/0167-577X(93)90082-9
34. Suzuki M, Kagawa M, Syono Y, Hirai T, Watanabe K (1992) Superconducting thin films of Bi–Pb–Sr–Ca–Cu–O synthesized by the spray-inductively coupled plasma technique. J Mater Sci 26(21):5929–5932. doi:10.1007/BF01130136
35. Shimada S, Yoshimatsu M, Nagai H, Suzuki M, Komaki H (2000) Preparation and properties of TiN and AlN films from alkoxide solution by thermal plasma CVD method. Thin Solid Films 370(1–2):137–145. doi:10.1016/S0040-6090(00)00935-4
36. Shimada S, Yoshimatsu M (2000) Preparation of $(Ti_{1-x}Al_x)N$ films from mixed alkoxide solutions by plasma CVD. Thin Solid Films 370(1–2):146–150. doi:10.1016/S0040-6090(00)00934-2
37. Takahashi M, Shimada S (2004) Preparation of composite and compositinally graded TiC–TiN films by liquid injection plasma-enhanced CVD. Solid State Ionics 172(1–4):249–252. doi:10.1016/j.ssi.2004.03.015
38. Shimada S, Tsukurimichi K (2000) Preparation of SiNx and composite $SiN_x$–TiN films from alkoxide solutions by liquid injection plasma CVD. Thin Solid Films 419(1–2):54–59. doi:10.1016/S0040-6090(02)00768-X
39. Shimada S, Fuji Y, Tsujino J, Yamazaki I (2010) Thermal plasma CVD and wear resistance of double layered Ti–Si–B–C/Ti–B–C coatings on WC–Co cutting tools with various roughness. Surf Coat Technol 204(11):1715–1721. doi:10.1016/j.surfcoat.2009.10.056
40. Ishigaki T, Oh SM, Li JG, Park DW (2005) Controlling the synthesis of TaC nanopowders by injecting liquid precursor into RF induction plasma. Sci Technol Adv Mater 6(2):111–118. doi:10.1016/j.stam.2004.11.001
41. Li JG, Ikeda M, Tang C, Moriyoshi Y, Hamanaka H, Ishigaki T (2007) Chlorinated nanocrystalline $TiO_2$ powders via one-step $Ar/O_2$ radio frequency thermal plasma oxidizing mists of $TiCl_3$ solution: phase structure and photocatalytic performance. J Phys Chem C 111(49):18018–18024. doi:10.1021/jp077320q
42. Ikeda M, Li JG, Kobayashi N, Moriyoshi Y, Hamanaka H, Ishigaki T (2008) Phase formation and luminescence properties in $Eu^{3+}$-doped $TiO_2$ nanoparticles prepared by thermal plasma pyrolysis of aqueous solutions. Thin Solid Films 516(19):6640–6644. doi:10.1016/j.tsf.2007.11.037
43. Li JG, Kamiyama H, Wang XH, Moriyoshi Y, Ishigaki T (2006) $TiO_2$ nanopowders via radio-frequency thermal plasma oxidation of organic liquid precursors: synthesis and characterization. J Eur Ceram Soc 26(4–5):423–428. doi:10.1016/j.jeurceramsoc.2005.07.034
44. Li JG, Ishigaki T, Ikeda M, Ye R, Moriyoshi Y (2007) Control of particle size and phase formation of $TiO_2$ nanoparticles synthesized in RF induction plasma. J Phys D Appl Phys 40(8):2348–2353. doi:10.1088/0022-3727/40/8/S14
45. Bouyer E, Gitzhofer F, Boulos MI (1997) The suspension plasma spraying of bioceramics by induction plasma. JOM 49(2):58–62. doi:10.1007/BF02915483
46. Soucy G, Rahmane M, Fan X, Ishigaki T (2001) Heat and mass transfer during in-flight nitridation of molybdenum disilicide in an induction plasma reactor. Mater Sci Eng, A 300(1–2):226–234. doi:10.1016/S0921-5093(00)01767-6
47. Li YL, Ishigaki T (2002) Thermodynamic analysis of nucleation of anatase and rutile from $TiO_2$ melt. J Cryst Growth 242(3–4):511–516. doi:10.1016/S0022-0248(02)01438-0
48. Wang XH, Li JG, Kamiyama H, Katada M, OhashiN Moriyoshi Y, Ishigaki T (2005) Pyrogenic iron(III)-doped $TiO_2$ nanopowders synthesized in RF thermal plasma: phase formation, defect structure, band gap, and magnetic properties. J Am Chem Soc 127(31):10982–10990. doi:10.1021/ja051240n
49. Li YL, Ishigaki T (2004) Controlled one-step synthesis of nanocrystalline anatase and rutile $TiO_2$ powders by in-flight thermal plasma oxidation. J Phys Chem B 108(40):15536–15542. doi:10.1021/jp040316j
50. Li JG, Wang XH, Watanabe K, Ishigaki T (2006) Phase structure and luminescence properties of $Eu^{3+}$-doped $TiO_2$ nanocrystals synthesized by $Ar/O_2$ radio frequency thermal plasma oxidation of liquid precursor mists. J Phys Chem B 110(3):1121–1127. doi:10.1021/jp053329l
51. Li JG, Wang XH, Tang C, Ishigaki T, Tanaka S (2008) Energy transfer enables 1.53 μm photoluminescence from erbium-doped $TiO_2$ semiconductor nanocrystals synthesized by $Ar/O_2$ radio-frequency thermal plasma. J Am Ceram Soc 91(6):2032–2035. doi:10.1111/j.1551-2916.2008.02318.x
52. Li JG, Büchel R, Isobe M, Mori T, Ishigaki T (2009) Cobalt-doped $TiO_2$ nanocrystallites: radio-frequency thermal plasma processing, phase structure, and magnetic properties. J Phys Chem C 113(19):8009–8015. doi:10.1021/jp8080047
53. Yamaura K, Wang XH, Li JG, Ishigaki T, Takayama-Muromachi E (2006) Magnetic properties of the highly iron-doped rutile $TiO_2$ nano crystals. Mater Res Bull 41(11):2080–2087. doi:10.1016/j.materresbull.2006.04.003

54. Tachikawa T, Ishigaki T, Li JG, Fujitsuka M, Majima T (2008) Defect-mediated photoluminescence dynamics of Eu3 + -doped $TiO_2$ nanocrystals revealed at the single-particle or single-aggregate level. Angew Chem Int Ed 47(29):5348–5352. doi:10.1002/anie.200800528
55. Zhang CN, Ikeda M, Uchikoshi T, Li JG, Watanabe T, Ishigaki T (2011) High-concentration niobium(V) doping into $TiO_2$ nanoparticles synthesized by thermal plasma processing. J Mater Res 26(5):658–671. doi:10.1557/jmr.2011.16
56. Zhang C, Uchikoshi T, Li JG, Watanabe T, Ishigaki T (2011) Influence of niobium doping on phase composition and defect-mediated photoluminescence properties of $Eu^{3+}$-doped $TiO_2$ nanopowders synthesized in $Ar/O_2$ thermal plasma. J Alloys Compd 509(36):8944–8951. doi:10.1016/j.jallcom.2011.06.089
57. Fujishima A, Honda K (1972) Electrochemical photolysis of water at a semiconductor electrode. Nature 238(5358):37–38. doi:10.1038/238037a0
58. Wang XH, Li JG, Kamiyama H, Moriyoshi Y, Ishigaki T (2006) Wavelength-sensitive photocatalytic degradation of methyl orange in aqueous suspension over iron(III)-doped $TiO_2$ nanopowders under UV and visible light irradiation. J Phys Chem B 110(13):6804–6809. doi:10.1021/jp060082z
59. Zhang CN, Ikeda M, Uchikoshi T, Li JG, Watanabe T, Ishigaki T (2011) Photocatalytic performance of iron (III) and niobium (V)-codoped $TiO_2$ nanopowders synthesized by a radio frequency thermal plasma process. Thin Solid Films 519(20):6940–6943. doi:10.1016/j.tsf.2010.11.050
60. Zhang CN, Uchikoshi T, Li JG, Watanabe T, Ishigaki T (2014) Photocatalytic activities of europium (III) and niobium (V) co-doped $TiO_2$ nanopowders synthesized in $Ar/O_2$ radio-frequency thermal plasmas. J Alloys Compd 606:37–43. doi:10.1016/j.jallcom.2014.03.191
61. Skandan G, Foster CM, Frase H, Ali MN, Parker JC, Hahn H (1992) Phase characterization and stabilization due to grain size effects of nanostructured $Y_2O_3$. Nanostruct Mater 1(4):313–322. doi:10.1016/0965-9773(92)90038-Y
62. Li JG, Ishigaki T (2012) One-step $Ar/O_2$ thermal plasma processing of $Y_2O_3$:$Eu^{3+}$ red phosphors: phase structure, photoluminescent properties, and the effects of $Sc^{3+}$ codoping. J Solid State Chem 196:58–62. doi:10.1016/j.jssc.2012.08.004
63. Kobayashi N, Ishigaki T, Watanabe T, Li JG (2011) Synthesis of pure, crystalline (Ba, Sr)$TiO_3$ nanosized powders in radio frequency induction thermal plasma. Int J Appl Ceram Technol 8(5):1125–1135. doi:10.1111/j.1744-7402.2010.02546.x
64. Sato K, Li JG, Kamiya H, Ishigaki T (2008) Ultrasonic dispersion of $TiO_2$ nanoparticles in aqueous suspension. J Am Ceram Soc 91(8):2481–2487. doi:10.1111/j.1551-2916.2008.02493.x
65. Sato K, Ikeda M, Li JG, Kamiya H, Ishigaki T (2011) Highly dispersed behavior of thermal plasma-synthesized $TiO_2$ nanoparticles in water. J Ceram Soc Jpn 119(4):303–306. doi:10.2109/jcersj2.119.303